Observation of the Three-Dimensional Polarization Vector in Films of Organic Molecular Ferroelectrics Using Terahertz Radiation Emission

Yuto Kinoshita,[1] Masato Sotome,[1] Tatsuya Miyamoto,[1] Yohei Uemura,[2] Shunto Arai,[2] Sachio Horiuchi,[3] Tatsuo Hasegawa,[2] Hiroshi Okamoto,[1,4] and Noriaki Kida[1,*]

[1] *Department of Advanced Materials Science, The University of Tokyo, 5-1-5 Kashiwa-no-ha, Chiba 277-8561, Japan*

[2] *Department of Applied Physics, The University of Tokyo, Tokyo 113-8656, Japan*

[3] *Research Institute for Advanced Electronics and Photonics (RIAEP), National Institute of Advanced Industrial Science and Technology (AIST), Tsukuba, Ibaraki 305-8565, Japan*

[4] *AIST-UTokyo Advanced Operando-Measurement Technology Open Innovation Laboratory (OPERAND-OIL), National Institute of Advanced Industrial Science and Technology (AIST), Chiba 277-8568, Japan*

For the application of a ferroelectric thin film to optical and electric devices, it is important to align its ferroelectric polarization parallel or perpendicular to the film surface. In this context, an effective method to characterize the polarization directions in the whole area of devices is needed. Here, we report an alternative method to determine a polarization vector in three dimensions using an emission of terahertz waves. The target material is an organic hydrogen-bonded molecular ferroelectric 2-methylbenzimidazole (MBI). By the irradiation of a femtosecond laser pulse on a bulk single-crystal thin film of MBI, we observe the emission of the terahertz waves originating from the polarization modulation of infrared-active phonons via the impulsive stimulated Raman-scattering mechanism. By measuring the terahertz electric field parallel to the ferroelectric polarization with rotating the single-crystal film around two independent axes, we succeed in determining the polarization vector in three dimensions, the direction of which is tilted by 45° normal to the film surface and substrate. This method can be a powerful tool to characterize directions of ferroelectric polarizations in any kinds of thin-film samples.

I. INTRODUCTION

Recent developments in printing techniques using organic ferroelectrics have opened an alternative possibility for their various applications such as capacitors, (piezoelectric) actuators, and memories [1]. To use organic ferroelectrics in thin films, it is important to characterize the orientations of ferroelectric polarizations. In most ferroelectric memory devices such as ferroelectric random access memories (FeRAMs) [2], the ferroelectric polarization of the film is normal to the substrate. One of the main reasons is that the switching voltage for the polarization reversal can be minimized in that configuration.

To explore the possibility of the applications to ferroelectric memories, several kinds of ferroelectric thin films [3–11] have been fabricated using organic molecular materials with a large spontaneous polarization [12,13]. It was suggested that a thin film of an organic molecular ferroelectric, 2-methylbenzimidazole (MBI) [6]

and 1,4-diazabicyclo[2.2.2]octan-1-ium tetrafluoroborate (Hdabco-BF4) [9], was superior to an inorganic thin film of $Pr(Zr, Ti)O_3$ in terms of the low-voltage operation. To characterize the quality of a thin film of ferroelectric materials, it is indispensable to measure the direction of polarization and its distribution over the whole sample. Particularly, in a ferroelectric memory, it is crucial to evaluate the polarization component normal to the film and substrate. For this purpose, a commercially available piezoresponse force microscopy (PFM) is sometimes used. However, PFM is surface sensitive but not bulk sensitive. Moreover, in PFM it is difficult to detect the polarization vector over a whole area of the film with a 1-mm^2 size. Thus, an effective method to determine the polarization vector in three dimensions over the macroscopic scale is highly desirable.

Recently, we found the emission of the terahertz wave radiated from hydrogen-bonded molecular ferroelectric crystals upon irradiation of a femtosecond laser pulse [14]; the amplitude and the sign of an electric field waveform of the terahertz radiation reflect the magnitude and direction of the ferroelectric polarization, respectively.

The mechanism of the terahertz radiation is explained as follows. When a femtosecond laser pulse is incident to a ferroelectric, the second-order nonlinear polarization $P^{(2)}$, which is described by the second-order nonlinear optical susceptibility $\chi^{(2)}$, can be modulated and the time-dependent component $\Delta P^{(2)}(t)$ of the polarization appears [15]. This component $\Delta P^{(2)}(t)$ generates an electromagnetic wave in the terahertz region via the electric dipole radiation [16]. The electric field waveform $E_{\text{THz}}(t)$ of the radiated electromagnetic wave is proportional to the second time derivative of $\Delta P^{(2)}(t)$ as $E_{\text{THz}}(t) \propto (\partial^2/\partial t^2)\Delta P^{(2)}(t)$. A well-known mechanism for the modulation of $P^{(2)}$ is a difference frequency generation (DFG) within an incident femtosecond laser pulse, which is sometimes called an optical-rectification (OR) mechanism [17]. The terahertz radiations observed in various kinds of hydrogen-bonded molecular ferroelectric crystals having π-electron systems such as 4,5-dihydroxy-4-cyclopenten-1,2,3-trione (croconic acid) [14], 2-phenylmalondialdehyde [18], and 4-[4-(methylthio)phenyl]-2,6-di(1*H*-pyrazol-1-yl)pyridine (UOH1) [19] have been explained by this OR mechanism. In the OR processes, $\Delta P^{(2)}(t)$ is proportional to the envelope function of the intensity of an incident laser pulse. Therefore, a nearly monocyclic electromagnetic wave is radiated and the spectrum of the electric field, $E_{\text{THz}}(\omega)$, is very broad.

Besides this, a polarization modulation by an infrared-active phonon is also known as an effective mechanism of the terahertz radiation. So far, two mechanisms of the terahertz radiations by phonons are proposed. One is the generation of the coherent longitudinal optical (LO) phonons of the infrared-active modes [20]. The generated coherent phonons can modulate $P^{(2)}(t)$, resulting in the emission of a multicyclic electromagnetic wave. This mechanism was widely observed in optically opaque inorganic semiconductors such as Te [21] and (Pb, Cd)Te [22]. The other is the generation of the coherent phonons of the Raman active modes via the impulsive stimulated Raman-scattering (ISRS) process [23]. In this case, $P^{(2)}(t)$ is proportional to both the polarizability of Raman scattering and the dipole moment of a specific phonon, so that $E_{\text{THz}}(\omega)$ shows a sharp peak structure at phonon frequency and $E_{\text{THz}}(t)$ has a multicyclic electric field. The terahertz radiation by this mechanism was observed in optically transparent compounds such as TeO_2 [24] and hydrogen-bonded molecular crystal, 5, 6-dichloro-2-methylbenzimidazole (DCMBI) [25].

In the present study, we report an evaluation method of the polarization vector in three dimensions in a thin-film sample of an organic molecular ferroelectric using the terahertz radiation induced by a femtosecond laser pulse. The studied material is MBI, in which the terahertz radiation by the ISRS mechanism is observed. By measuring the amplitudes of the terahertz electric fields with

rotating the sample, we determine the orientation of the polarization.

MBI is one of the hydrogen-bonded molecular crystals having π-electron systems, which show the ferroelectricity at room temperature [26]. According to the recent x-ray diffraction analysis [26], the crystal system of MBI is monoclinic with the space group of Pn, and has pseudotetragonal $P4_2/n$ symmetry [27]. Figure 1(a) shows the schematic of the crystal structure of MBI. Each MBI molecule has the asymmetric π-electron system and carries a large dipole moment. Those molecules are connected by the hydrogen bonds (dotted lines) and protons are located at the off-center proton positions. As a result, the polarization of chain P_{proton} appears along the direction parallel to the hydrogen bonds, and its direction can be switched by the electric field. In real crystals, the molecular chains, which are schematically shown in Fig. 1(b), are
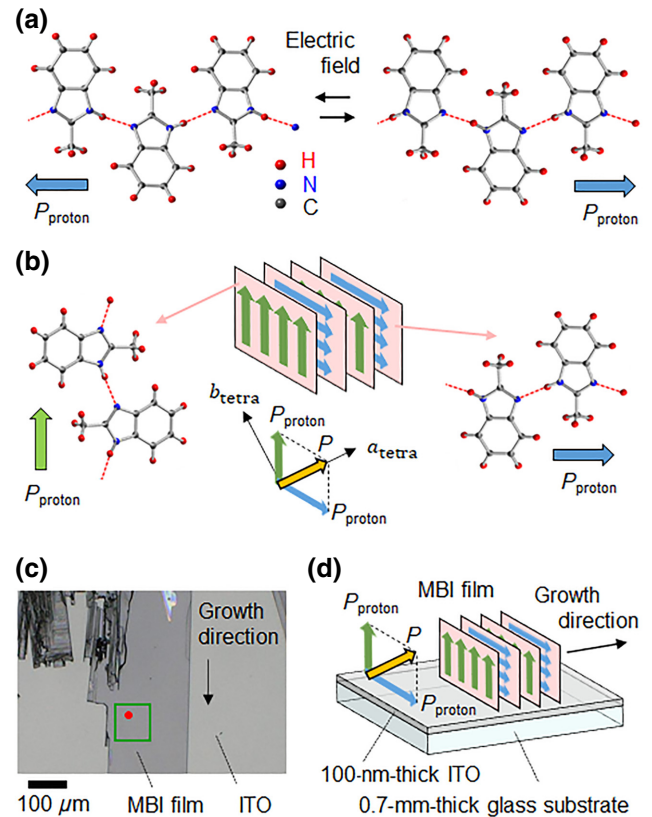

FIG. 1. (a) Crystal structure of MBI. The polarization of chain P_{proton} originating from the proton ordering in the $N-H-N$ bonds (dotted lines) is indicated by an arrow. P_{proton} can be switched by the electric field. (b) In real crystals, the microscopic polarization P appears along the orthogonal direction, which is parallel to the a axis (a_{tetra}) or the b axis (b_{tetra}) in the tetragonal setting. (c) Optical image of MBI film. The homogeneous distribution of the polarization is confirmed by PFM in the area indicated by the green box. The red circle indicates the spot size of a femtosecond laser pulse. (d) Schematic of the prepared MBI film.

two dimensionally aligned. In two adjacent molecular layers, the directions of the molecular chains are different by 90°, resulting in the macroscopic polarization P along two orthogonal directions, i.e., parallel to the a axis (a_{tetra}) or the b axis (b_{tetra}) in the tetragonal setting [26] and thus MBI is a biaxial ferroelectric. In the PFM image of a single crystal, 90° domains and domain walls are indeed discerned [26].

II. EXPERIMENTAL SETUP

The (110)-oriented bulk single crystals of MBI are prepared by a previously reported method [26]. In films, the solvent of MBI single crystals are sandwiched by a 0.7-mm-thick silicon dioxide substrate and a thinner cover plate, as reported previously [6,11]. In order to apply the voltage normal to the film, 100-nm-thick indium tin oxide (ITO) is deposited on one side of the substrates. ITO can act as an electrode for PFM measurements and it is transparent to a femtosecond laser pulse with 800 nm used in the terahertz-radiation experiments. After the solvent is evaporated, the elongated flakelike crystals are grown on part of the substrate, the optical image of which is shown in Fig. 1(c). They are grown in the lateral direction, which is indicated by an arrow, and their width is about 100 μm. In this image, an optically homogeneous area of the crystal with about $200 \times 200 \, \mu\text{m}^2$ is discerned. In the restricted area ($90 \times 90 \, \mu\text{m}^2$) indicated by the green box, we confirm the homogenous distribution of the polarization by the out-of-plane PFM measurements, indicating the formation of a single-domain structure. We confirm that the polarization direction is tilted by 45° relative to the substrate [6], which is schematically shown in Fig. 1(d). The film thickness is estimated to be 4 μm by atomic force microcopy (AFM).

In the terahertz-radiation experiments, we use a femtosecond laser pulse (the center wavelength of 800 nm, the pulse width of 100 fs, and the repetition rate of 80 MHz), which is incident normal to the ITO side of the sample. The emitted terahertz electric field is detected by a low-temperature-grown GaAs photoswitch. By using two-wire grid polarizers placed in front of the detector [14], we measure polarized waveforms of terahertz electric fields.

In Raman spectroscopy and transmission experiments in the terahertz region, we use bulk single crystals. In Raman spectroscopy, a cw He-Ne laser as the light source and a grating monochromator equipped with a CCD camera are adopted. By using standard terahertz time-domain spectroscopy [28], we measure the transmission spectrum and calculate the complex optical constants.

All the measurements are performed at room temperature.

III. RESULTS AND DISCUSSION

A. Terahertz radiation using single crystals

First, we show the results of terahertz-radiation experiments using bulk single crystals. Since the

penetration depth of a femtosecond laser pulse (approximately 8.3 mm at 800 nm) exceeds the typical sample thickness (approximately 120 μm), attenuation of a laser pulse within the sample is negligible. The electric fields of the femtosecond laser pulses E_{ex}^{ω} and the detected terahertz waves are set parallel to the a_{tetra}, $E_{\text{ex}}^{\omega} \parallel a_{\text{tetra}}$, and $E_{\text{THz}} \parallel a_{\text{tetra}}$, which is schematically shown in the inset of Fig. 2(a). Figure 2(a) shows the detected waveform of the terahertz electric field $E_{\text{THz}}(t)$ radiated from the crystal. The time origin (0 ps) is set at the time when the absolute value of $E_{\text{THz}}(t)$ becomes a maximum. A prominent oscillation signal, which seems to consist of several oscillatory components, is discerned. To clearly see these components, we show in Fig. 2(b) by the green line the fast Fourier-transformed (FFT) spectrum of the obtained $E_{\text{THz}}(t)$ profile, $E_{\text{THz}}(\omega)$. Two peak structures are clearly
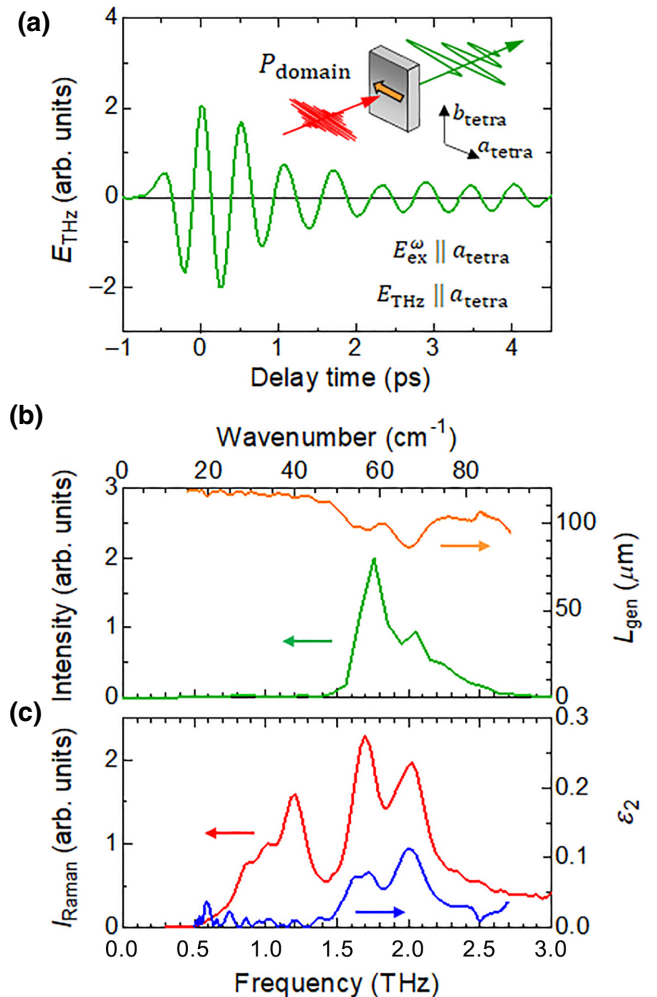
FIG. 2. (a) Terahertz electric field waveforms in bulk MBI single crystals obtained for $E_{\text{ex}}^{\omega} \parallel a_{\text{tetra}}$ and $E_{\text{THz}} \parallel a_{\text{tetra}}$. (b) Its fast Fourier-transformed power spectrum and effective generation length for terahertz radiations L_{gen}. (c) Raman and imaginary part of dielectric spectra in the bulk MBI single crystal.

observed at 1.75 and 2.03 THz with the frequency resolution of 0.1 THz. Appearance of these peak structures cannot be explained by the conventional OR mechanism but is attributable to the phonon-generation mechanism.

In order to demonstrate the phonon-generation mechanism for the observed terahertz radiation, we measure the Raman scattering I_{Raman} spectrum in a back-scattering geometry. Figure 2(c) shows I_{Raman} obtained for $E_{\mathrm{in}}^{\omega} \parallel a_{\mathrm{tetra}}$ and $E_{\mathrm{out}}^{\omega} \parallel b_{\mathrm{tetra}}$ (a red line), in which the electric field of the incident and detected light is orthogonal ($E_{\mathrm{in}}^{\omega} \perp E_{\mathrm{out}}^{\omega}$). The sharp five Raman-active phonon modes are discerned at 0.85, 1.00, 1.20, 1.70, and 2.05 THz within the frequency resolution of 0.03 THz. According to the Raman selection rule with the space group Pn, $A'(x,z)$ TO mode is active for $E_{\mathrm{in}}^{\omega} \perp E_{\mathrm{out}}^{\omega}$ and thus the observed modes are assigned to $A'(x,z)$ TO modes. The peak frequencies of two of them (at 1.70 and 2.05 THz) nearly correspond to those observed in $E_{\mathrm{THz}}(\omega)$.

To further get insight into the observed Raman-active phonon modes, we perform terahertz time-domain spectroscopy using a single-crystal sample with the thickness of 430 μm and measure the complex transmission spectrum in the terahertz region. The blue line in Fig. 2(c) shows the imaginary part of the dielectric constant ε_2 spectrum, which is numerically derived from the experimentally determined complex transmission spectrum, the detail of our calculation procedure is reported in Ref. [24]. The infrared-active TO modes are observed at 1.60, 1.75, and 2.05 THz in the measured frequency range. Thus, we conclude that two peak structures appeared in $E_{\mathrm{THz}}(\omega)$ are both Raman- and infrared-active TO modes

When the spectral width of the incident femtosecond laser pulse (approximately 5 THz) exceeds the frequency of Raman-active phonons, they are coherently excited and produce oscillations of the nonlinear polarizations, resulting in narrowband terahertz radiations. This process is called ISRS [23]. The time-dependent amplitude $Q(t)$ of the phonon mode is given by $Q(t) = \int_{-\infty}^{t} dt' G_{11}(t - t') R_{jk} E_j(t') E_k^*(t')$ [23]. Here, G_{11} is a Green function, R_{jk} is a Raman tensor, and E is an electric field. By taking into account the conservation law of the wavevector, the frequency-dependent amplitude $Q(\omega)$ of the phonon mode is given by $Q(\omega) \propto R_{jk} E_j(\omega) E_k^*(\omega)$ [23]. The nonlinear polarization $P_i(\omega)$ originating from the ISRS is represented by $P_i(\omega) \propto \mu_i R_{jk} E_j(\omega) E_k^*(\omega)$, where μ_i is the dipole moment. Thus, in ISRS mechanism of terahertz radiation, the related phonon modes are both Raman and infrared active, which is detailed in the previous studies of TeO_2 [24] and DCMBI [25]. In the case of the ferroelectrics such as MBI, μ_i is proportional to the spontaneous polarization, and thus the terahertz radiation is related to the spontaneous polarization. Indeed, we successfully detected the ferroelectric domains and domain walls in other organic ferroelectric, DCMBI by

using terahertz radiations originating from the ISRS [25]. In MBI investigated here, as seen in Figs. 2(b) and 2(c), the central frequencies of the peak structures observed in the terahertz-radiation spectrum correspond with those of Raman and infrared-active phonon modes, which are clarified by Raman and infrared (terahertz time-domain) spectroscopies, respectively. Thus, we conclude that the terahertz radiation observed in MBI originates from the infrared-active phonons excited via ISRS processes.

B. Principle of evaluation method of polarization vector

Here, we describe the basic principle of an evaluation method of the polarization vector in three dimensions by an emission of terahertz radiations. Recently, we found the emission of the terahertz radiations in various organic ferroelectrics and observed the amplitude and sign of $E_{\mathrm{THz}}(0)$ correspond to the magnitude and direction of the ferroelectric polarization, respectively [14]. By using these unique characteristics, we successfully visualize the ferroelectric domains and domain walls by measuring the position dependence of $E_{\mathrm{THz}}(0)$ [14,25,29,30]. In this work, we also use these characteristics. Since $E_{\mathrm{THz}}(0)$ depends on the polarization direction, it is possible to detect the polarization vector by measuring $E_{\mathrm{THz}}(0)$ from various directions in three dimensions.

Next, we explain in detail the polarization position in the experimental geometry, which is shown in Fig. 3(a). We define the polar coordinates x, y, and z, with respect to the polarization orientation. $\psi (0 \le \psi \le \pi)$ is the angle from the y axis and $\xi (0 \le \xi \le 2\pi)$ is the azimuthal angle from the z axis within the x-z plane. In this case, a unit vector **n** is given by $\mathbf{n} = (\sin\psi \sin\xi, \cos\psi, \sin\psi \cos\xi)$. We consider the rotation of the sample around x, y, and z axes, which is schematically shown in Fig. 3(b). Using rotation matrices with respect to the x, y, and z axes, R_x, R_y, R_z, we obtain the polarization components polarized parallel to the x, y, and z axes, P_x, P_y, P_z. When the sample is rotated with the angle θ about the z axis, as shown in Fig. 3(c), the polarization
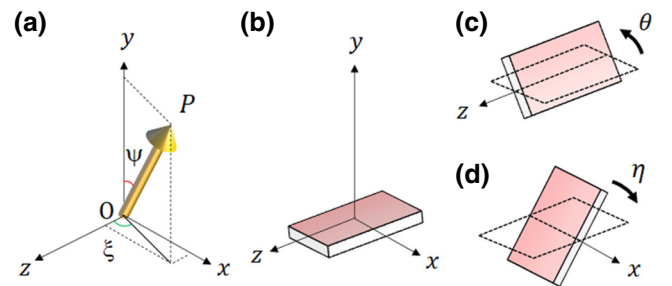

FIG. 3. (a) Polarization direction in the polar coordinates. Schematics of (b) sample geometry with the angle θ about the z axis (c) and the angle η about the x axis (d).

components are given by

$$\begin{pmatrix} P_x \\ P_y \\ P_z \end{pmatrix} \propto R_z(\theta)\mathbf{n} = \begin{pmatrix} \sin\psi \sin\xi \cos\theta - \cos\psi \sin\theta \\ \sin\psi \sin\xi \sin\theta + \cos\psi \cos\theta \\ \sin\psi \cos\xi \end{pmatrix}. \quad (1)$$

When the detector polarization is set to parallel to the x axis, P_x can be obtained. In the case of the sample rotation with the angle η about the x axis, which is shown in Fig. 3(d), the polarization components are given by

$$\begin{pmatrix} P_x \\ P_y \\ P_z \end{pmatrix} \propto R_x(\eta)\mathbf{n} = \begin{pmatrix} \sin\psi \sin\xi \\ \cos\psi \cos\eta - \sin\psi \cos\xi \sin\eta \\ \cos\psi \sin\eta + \sin\psi \cos\xi \cos\eta \end{pmatrix}. \quad (2)$$

If the emission of terahertz radiations polarized along the polarization direction is dominant, we can determine ψ and ξ by measuring θ and η dependences of $E_{\mathrm{THz}}(0)$.

C. Terahertz radiation using single-crystal films

Next, we show the results of terahertz-radiation experiments using bulk single-crystal films and demonstrate an evaluation method of the polarization vector in three dimensions. As described above, in a form of thin films, the polarization direction is tilted by 45° relative to the substrate [6]. In this case, ξ shown in Fig. 3(a) is 90°. Here, we define the laboratory coordinate x, y, and z, with respect to the sample orientation as shown in Fig. 4(a). The electric field of the femtosecond laser pulse is set parallel to the x axis, i.e., $E_{\mathrm{ex}}^{\omega} \parallel x$. By using a rotating stage, the sample is rotated by an angle θ with respect to the z axis. $\theta = 0$ corresponds to the sample surface parallel to the x axis. Figure 4(b) shows the waveforms of the terahertz electric field obtained for $E_{\mathrm{THz}} \parallel x$ and $E_{\mathrm{THz}} \parallel z$ when $\theta = -41°$. The spot diameter of the laser pulse is 25 μm, which is indicated by the closed red circle in Fig. 1(c). In $E_{\mathrm{THz}} \parallel x$, we observe an emission of the terahertz wave (E_{THz}^x), which consists of oscillatory components with different frequencies. On the other hand, in the detected electric field for $E_{\mathrm{THz}} \parallel z$, E_{THz}^z, is negligibly small. This clearly indicates
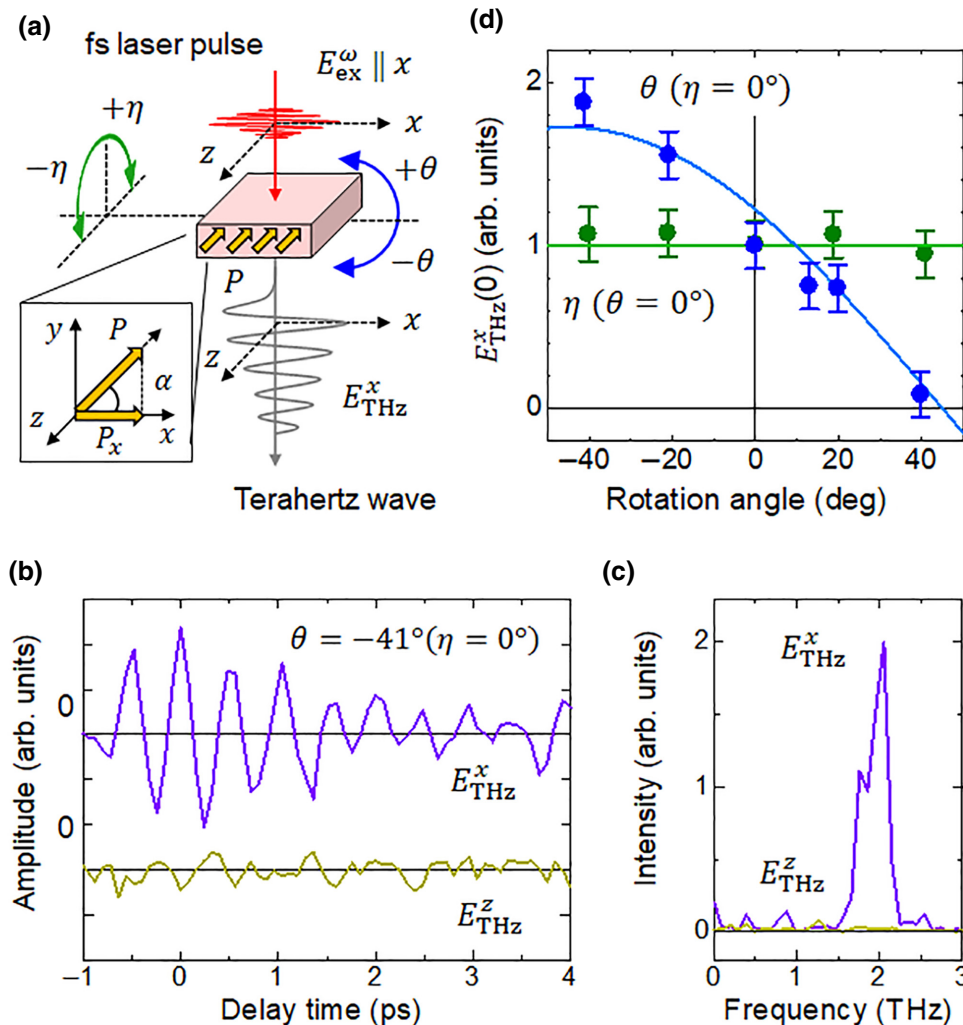

FIG. 4. (a) Schematic of the terahertz-radiation measurement on MBI film. (b) Terahertz electric field waveforms in MBI film obtained for E^x_{THz} and E^z_{THz} when the electric field of the incident femtosecond laser pulse is set parallel to the x axis. (c) Their FFT power spectra. (d) $E^x_{\mathrm{THz}}(0)$ as a function of the rotation angle θ and η.

that the polarization P of the sample is within the x-y plane, which is schematically shown in the box in Fig. 4(a). Thus, the magnitude of the terahertz electric field obtained at the time origin, $E_{THz}^x(0)$, is proportional to the x-axis component of the polarization P of the sample. Here, we define the angle α of P relative to the x axis. Thus, $E_{THz}^x(0)$ is proportional to $\cos\alpha$.

In order to clarify the nature of the terahertz radiations from the film, we perform the FFT of the measured $E_{THz}^x(t)$ and $E_{THz}^z(t)$ profiles. The obtained power spectra $E_{THz}^x(\omega)$ and $E_{THz}^z(\omega)$ are shown by the purple and yellow lines in Fig. 4(c), respectively. The frequency resolution is 0.1 THz. At least two peak structures at 1.7 and 2.0 THz are discerned in $E_{THz}^x(\omega)$, being consistent with the results obtained in bulk single crystals shown in Fig. 2(b). In contrast, there are no remarkable peak structures in $E_{THz}^z(\omega)$.

D. Observation of the relative orientation of the polarization vector using terahertz radiation

Now, we proceed to discuss the method for the determination of the relative orientation of the polarization vector. As discussed above, $E_{THz}^x(0)$ is proportional to $\cos\alpha$. In order to estimate α, we measure $E_{THz}^x(0)$ as a function of θ, which is shown by blue circles in Fig. 4(d). $E_{THz}^x(0)$ is normalized by $E_{THz}^x(0)$ at $\theta = 0°$. $E_{THz}^x(0)$ becomes a maximum at $\theta \sim -45°$ and nearly zero at $\theta \sim +45°$. By assuming that $E_{THz}^x(0)$ is proportional to the P along the x axis, $E_{THz}^x(0)$ can be expressed as $E_{THz}^x(0) \sim \cos(\theta + \alpha)$, which is obtained from P_x in Eq. (1) for $\xi = 90°$ and $\alpha + \psi = 90°$. The observed $E_{THz}^x(0)$ can be well fitted by this relationship with $\alpha = +45°$, which is shown by the solid blue line in Fig. 4(d).

We also rotate the sample by η with respect to the x axis, while θ is fixed to $\theta = 0°$, which is schematically shown in Fig. 4(a). The measured $E_{THz}^x(0)$ as a function of η is

shown by the green circles in Fig. 4(d). $E_{THz}^x(0)$ is independent of η, which is consistent with the expected value, i.e., constant, of P_x in Eq. (2) for $\xi = 90°$ and $\alpha + \psi = 90°$. This clearly indicates that P is only declined from the x axis by $\alpha = +45°$ and perpendicular to the z axis. This is consistent with the rotation experiments (θ with $\eta = 0°$) with respect to the z axis shown by the blue circles in Fig. 4(d).

Next, the electric field of the incident light is set parallel to the z axis, i.e., $E_{ex}^\omega \parallel z$, and the emitted terahertz wave along the z axis is detected. The experimental setup is shown in Fig. 5(a). In this geometry, P along the y axis can be detected by rotating the substrate with respect to the x axis [see the box in Fig. 5(a)]. Figure 5(b) shows the $E_{THz}^z(0)$ as a function of η. $E_{THz}^z(0)$ is zero at $\eta = 0°$, while the absolute value of $E_{THz}^z(0)$ shows a monotonic increase to $\eta \sim \pm 45°$. This clearly indicates that P is parallel to the x-y plane and declined by $\alpha \sim +45°$ from the x axis. The observed $E_{THz}^z(0)$ can be well fitted by $E_{THz}^z(0) \sim \sin(\eta)$, which is obtained from P_z in Eq. (2) for $\xi = 90°$ and $\alpha + \psi = 90°$, as shown by the solid line in Fig. 5(b). On the basis of the θ and η dependences of the results presented above, we can conclude that the relative orientation of the ferroelectric polarization vector is tilted by 45° normal to the sample surface within the x-y plane, which is consistent with the previous PFM results on an MBI film [see, Fig. 1(d)] [6].

Since strong absorptions exist in the terahertz region [Fig. 2(c)], it is valuable to discuss the effective generation length for terahertz radiations $L_{gen}(\omega)$ [31]. $L_{gen} = \{1 + \exp(-\alpha_{abs}d) - 2\exp[-(\alpha_{abs}/2)d]\cos[(\omega/c)|n_{THz} - n_g|d]/(\alpha_{abs}/2)^2 + (\omega/c)^2(n_{THz} - n_g)^2\}^{\frac{1}{2}}$ is an effective propagation length within the crystal over which the coherence between the generated terahertz wave and the incident femtosecond laser pulse degrades. Here, c is a velocity of light, ω is an angular frequency, n_g ($=1.57$) is the group refractive index of the incident femtosecond laser pulse,

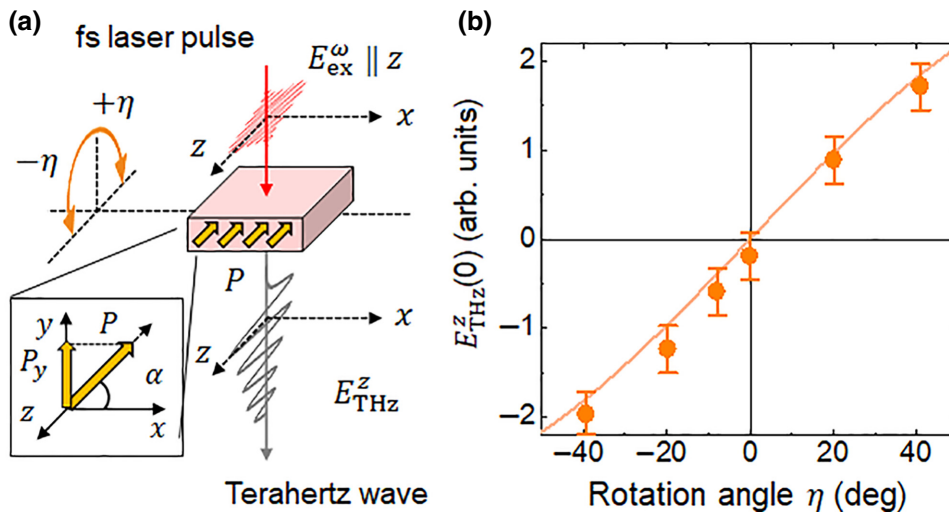

FIG. 5. (a) Schematic of terahertz-radiation measurement on MBI film. (b) Terahertz electric field obtained for $E^z{}_{THz}(0)$ as a function of the rotation angle η. The electric field of the incident femtosecond laser pulse is set parallel to the z axis.

d is the sample thickness of the single crystal (430 μm). n_{THz} and α_{abs} are the refractive index and absorption coefficient in the terahertz frequency region, respectively, which are determined by the terahertz time-domain spectroscopy. The estimated $l_{gen}(\omega)$ is shown by the orange line in Fig. 2(b). Although dip structures due to strong absorptions of the phonons are discerned at 1.7 and 2.0 THz, $L_{gen}(\omega)$ is estimated to be approximately 100 μm in the measured region, which is much longer than the thickness of the film (4 μm). The penetration depth of the femtosecond laser pulse (8.3 mm) is also long. Thus, as compared to the surface-sensitive PFM, the present terahertz-radiation method is a bulk sensitive. This characteristic is useful to evaluate the polarization component normal to the film in the FeRAMs.

Finally, we comment on the perspective of the present terahertz-radiation method. In the present work, we successfully determine the direction of the polarization in the single-domain samples. In the next step, we try to detect the unknown direction of the polarization in grain boundaries and multidomain samples. In order to achieve it, it is indispensable to improve the spatial resolution. In the present terahertz-radiation experiments, the spatial resolution corresponds to the spot size of the laser pulse (25 μm). Here, we use femtosecond laser pulses with a wavelength of 800 nm and the conventional lens. If the short-wavelength laser pulse and objective lens are used, higher spatial resolution would be achieved. However, the diffraction limit should be taken into account when the wavelength becomes shorter. A near-field imaging is known as a method for overcoming such a diffraction limit. In the terahertz region, a scattering-type near-field microscope using a metal tip has been recently developed [32] and obtained the spatial resolution of 20 nm. Using a near-field optics, it is possible to characterize grain boundaries and multidomain samples as well as the single-domain samples we demonstrate here. This technical issue is beyond the scope of the present work and will be performed in the future.

IV. SUMMARY

We develop an alternative method to determine the orientation of a macroscopic polarization vector in films of ferroelectrics using emission of terahertz radiation and demonstrate the effectiveness of the method using hydrogen-bonded molecular ferroelectric 2-methylbenzimidazole single-crystal films. By measuring the emitted terahertz electric fields with rotating the substrate of the film, we unambiguously determine the direction of the polarization to be tilted to a specific direction by 45° from the sample surface and substrate. The terahertz-radiation method we develop here is bulk sensitive and thus can be used to characterize ferroelectric properties in a whole area of a sample.

[1] S.-T. Han, Y. Zhou, and V. A. L. Roy, Towards the development of flexible non-volatile memories, Adv. Mater. **25**, 5425 (2013).

[2] J. F. Scott, *Ferroelectric Memories* (Springer-Verlag, Berlin, 2000).

[3] X.-L. Li, K. Chen, Y. Liu, Z.-X. Wang, T.-W. Wang, J.-L. Zuo, Y.-Z. Li, Y. Wang, J. S. Zhu, J.-M. Liu, Y. Song, and X.-Z. You, Molecule-based ferroelectric thin films: Mononuclear lanthanide enantiomers displaying room-temperature ferroelectric and dielectric properties, Angew. Chem. Int. Ed. **46**, 6820 (2007).

[4] Y. Zhang, Y. Liu, H.-Y. Ye, D.-W. Fu, W. Gao, H. Ma, Z. Liu, Y. Liu, W. Zhang, J. Li, G.-L. Yuan, and R.-G. Xiong, A molecular ferroelectric thin film of imidazolium perchlorate that shows superior electromechanical coupling, Angew. Chem. Int. Ed. **53**, 5064 (2014).

[5] W. Gao, L. Chang, H. Ma, L. You, J. Yin, J. Liu, Z. Liu, J. Wang, and G. Yuan, Flexible organic ferroelectric films with a large piezoelectric response, NPG Asia Mater. **7**, e189 (2015).

[6] Y. Noda, T. Yamada, K. Kobayashi, R. Kumai, S. Horiuchi, F. Kagawa, and T. Hasegawa, Few-volt operation of printed organic ferroelectric capacitor, Adv. Mater. **27**, 6475 (2015).

[7] K. Gao, C. Xu, Z. Cui, C. Liu, L. Gao, C. Li, D. Wu, H.-L. Cai, and X. S. Wu, The growth mechanism and ferroelectric domains of diisopropylammonium bromide films synthesized *via* 12-crown-4 addition at room temperature, Phys. Chem. Chem. Phys. **18**, 7626 (2016).

[8] X. Jiang, H. Lu, Y. Yin, X. Zhang, X. Wang, L. Yu, Z. Ahmadi, P. S. Costa, A. D. DiChiara, X. Cheng, A. Gruverman, A. Enders, and X. Xu, Room temperature ferroelectricity in continuous croconic acid thin films, Appl. Phys. Lett. **109**, 102902 (2016).

[9] P.-P. Shi, Y.-Y. Tang, P.-F. Li, H.-Y. Ye, and R.-G. Xiong, De novo discovery of [Hdabco]BF$_4$ molecular ferroelectric thin film for nonvolatile low-voltage memories, J. Am. Chem. Soc. **139**, 1319 (2017).

[10] Y.-Y. Tang, P.-F. Li, P.-P. Shi, W.-Y. Zhang, Z.-X. Wang, Y.-M. You, H.-Y. Ye, T. Nakamura, and R.-G. Xiong, Visualization of Room-Temperature Ferroelectricity and Polarization Rotation in the Thin Film of Quinuclidinium Perrhenate, Phys. Rev. Lett. **119**, 207602 (2017).

[11] Y. Uemura, S. Arai, J. Tsutsumi, S. Matsuoka, H. Yamada, R. Kumai, S. Horiuchi, A. Sawa, and T. Hasegawa, Field Modulation Imaging of Ferroelectric Domains in Molecular Single-Crystal Film, Phys. Rev. Appl. **11**, 014046 (2019).

[12] S. Horiuchi and S. Ishibashi, Hydrogen-bonded small-molecular crystals yielding strong ferroelectric and antiferroelectric polarizations, J. Phys. Soc. Jpn. **89**, 051009 (2020).

[13] A. S. Tayi, A. Kaeser, M. Matsumoto, T. Aida, and S. I. Stupp, Supramolecular ferroelectrics, Nat. Chem. **7**, 281 (2015).

[14] M. Sotome, N. Kida, S. Horiuchi, and H. Okamoto, Visualization of ferroelectric domains in a hydrogen-bonded molecular crystal using emission of terahertz radiation, Appl. Phys. Lett. **105**, 041101 (2014).

[15] Y. R. Shen, *The Principles of Nonlinear Optics* (Wiley, New York, 1984).

[16] M. Tonouchi, Cutting-edge terahertz technology, Nat. Photonics **1**, 9 (2007).

[17] M. Bass, P. A. Franken, J. F. Ward, and G. Weinreich, Optical Rectification, Phys. Rev. Lett. **9**, 446 (1962).

[18] W. Guan, N. Kida, M. Sotome, Y. Kinoshita, R. Takeda, A. Inoue, S. Horiuchi, and H. Okamoto, Terahertz radiation by optical rectification in a hydrogen-bonded organic molecular ferroelectric crystal, 2-phenylmalondialdehyde, Jpn. J. Appl. Phys. **53**, 09PD07 (2014).

[19] U. Venkataramudu, C. Sahoo, S. Leelashree, M. Venkatesh, D. Ganesh, S. R. G. Naraharisetty, A. K. Chaudhary, S. Srinathb, and R. Chandrasekar, Terahertz radiation and second-harmonic generation from a single-component polar organic ferroelectric crystal, J. Mater. Chem. C **6**, 9330 (2018).

[20] A. V. Kuznetsov and C. J. Stanton, Coherent phonon oscillations in GaAs, Phys. Rev. B **51**, 7555 (1995).

[21] T. Dekorsy, H. Auer, C. Waschke, H. J. Bakker, H. G. Roskos, H. Kurz, V. Wagner, and P. Grosse, Emission of Submillimeter Electromagnetic Waves by Coherent Phonons, Phys. Rev. Lett. **74**, 738 (1995).

[22] M. Tani, R. Fukasawa, H. Abe, S. Matsuura, K. Sakai, and S. Nakashima, Terahertz radiation from coherent phonons excited in semiconductors, J. Appl. Phys. **83**, 2473 (1998).

[23] T. P. Dougherty, G. P. Wiederrecht, and K. A. Nelson, Impulsive stimulated Raman scattering experiments in the polariton regime, J. Opt. Soc. Am. B **9**, 2179 (1992).

[24] M. Sotome, N. Kida, R. Takeda, and H. Okamoto, Terahertz radiation induced by coherent phonon generation via impulsive stimulated Raman scattering in paratellurite, Phys. Rev. A **90**, 033842 (2014).

[25] M. Sotome, N. Kida, S. Horiuchi, and H. Okamoto, Narrow-band terahertz radiation by impulsive stimulated Raman scattering in an above-room-temperature organic ferroelectric benzimidazole, Phys. Rev. A **98**, 013843 (2018).

[26] S. Horiuchi, F. Kagawa, K. Hatahara, K. Kobayashi, R. Kumai, Y. Murakami, and Y. Tokura, Above-room-temperature ferroelectricity and antiferroelectricity in benzimidazoles, Nat. Commun. **3**, 1308 (2012).

[27] A. E. Obodovskaya, Z. A. Starikova, S. N. Belous, and I. E. Pokrovskaya, Crystal and molecular structure of 2-methylbenzimidazole, J. Struct. Chem. **32**, 421 (1991).

[28] R. Takeda, N. Kida, M. Sotome, Y. Matsui, and H. Okamoto, Circularly polarized terahertz radiation from a eulytite oxide by a pair of femtosecond laser pulses, Phys. Rev. A **89**, 033832 (2014).

[29] M. Sotome, N. Kida, S. Horiuchi, and H. Okamoto, Terahertz radiation imaging of ferroelectric domain topology in room-temperature hydrogen-bonded supramolecular ferroelectrics, ACS Photonics **2**, 1373 (2015).

[30] M. Sotome, N. Kida, Y. Kinoshita, H. Yamakawa, T. Miyamoto, H. Mori, and H. Okamoto, Visualization of a nonlinear conducting path in an organic molecular ferroelectric by using emission of terahertz radiation, Phys. Rev. B **95**, 241102(R) (2017).

[31] A. Schneider, M. Neis, M. Stillhart, B. Ruiz, R. U. A. Khan, and P. Günter, Generation of terahertz pulses through optical rectification in organic DAST crystals: Theory and experiment, J. Opt. Soc. Am. B **23**, 1822 (2006).

[32] P. Klarskov, H. Kim, V. L. Colvin, and D. M. Mittleman, Nanoscale laser terahertz emission microscopy, ACS Photonics **4**, 2676 (2017).